Uncertainty in Large-Signal Measurements Under Variable Load Conditions

Konstanty Łukasik, Jerome Cheron, *Member, IEEE*, Gustavo Avolio, *Member, IEEE*, Arkadiusz Lewandowski, *Member, IEEE*, Dylan F. Williams, *Fellow, IEEE*, Wojciech Wiatr, *Member, IEEE*, and Dominique M. M.-P. Schreurs, *Fellow, IEEE*

***Abstract*—We investigate the uncertainty of large-signal measurements of a microwave transistor due to variation in the load conditions at the fundamental frequency. In particular, we evaluate uncertainties in the complex frequency-domain traveling voltage waves. In our analysis, uncertainty sources typical for large-signal measurements are considered. Then, we discuss how the resultant uncertainty in the waves is dependent on a varying load reflection coefficient. For this investigation, we consider total uncertainty of the waves as well as its magnitude and phase. We also show that these errors unavoidably affect uncertainty of performance quantities, like output power.**

***Index Terms*—Calibration, large-signal measurements, load-pull, measurement uncertainty, sensitivity analysis, vector network analyzer**

I. Introduction

LOAD-PULL measurements [1] extend large-signal measurement systems [2], [3] by changing the load conditions of a device under test (DUT). The most common setup only sets load impedance at the DUT excitation signal's fundamental frequency f_0. However, variants are also available that can control load conditions at harmonically related frequencies of f_0, usually at the second and third harmonic. A number of methods have been introduced over the years for setting the reflection coefficients. These solutions are based on both active [4], [5] and passive [6] load tuning. Moreover, a wideband load-pull system that is capable of controlling reflection coefficients for a modulated signal has been recently proposed [7]. Measurements taken with those setups can be used for a variety of purposes, including device modeling [8], model validation [9], and design of high-performance power amplifiers (PAs) [10].

Knowing the uncertainty in measurements is particularly important for achieving first pass microwave circuit design success [9], [11]. By using results with relevant uncertainties, it is possible to estimate whether a project is likely to be successful with only one development iteration. As load-pull measurements gain popularity, it is of great importance to provide microwave circuit designers with data on how credible the load-pull results are. This may result in speeding up the design process and shortening the time between an idea and a product release.

While the uncertainty in large-signal measurements has been extensively investigated [12]–[16], including time-domain waveform uncertainties, [16], there has been relatively little work on evaluating the uncertainty in load-pull measurements. The attempts [17], [18] have so far focused on power-related figures of merit, like power-added efficiency (PAE) or gain, derived from these measurements. uncertainty in the actual waves at the device's terminals was not considered. Furthermore, focus was only on the uncertainty of figures of merit in relation to the magnitude of the reflection coefficient Γ_L whereas its phase was not considered.

In this paper, we evaluate the uncertainty in the DUT's complex complex frequency-domain traveling voltage waves while considering both the magnitude and the phase of the load reflection coefficient. To achieve this goal, we performed extensive measurements and followed strict calibration schemes. We delineate sources of uncertainty in large-signal measurements and derive how they are included during a two-tier vector calibration using the Microwave Uncertainty Framework (MUF) developed at the National Institute of Standards and Technology (NIST) [19]. Next, we describe the measurement system used for taking load-pull measurements as well as a method for choosing load reflection coefficients. Finally, we evaluate uncertainty in the DUT's frequency-domain waves.

II. Uncertainty Analysis of Large-Signal Measurements

Evaluating measurement uncertainty is a complex challenge where many sources of errors, both random and systematic, must be included. By using the NIST MUF, we were able to consider uncertainties of the passive calibration standards, power meter, NIST traceable phase calibration reference [20],

Manuscript received June ?, 2019; revised ?.

This work was funded by FWO-Vlaanderen (Belgium) and KU Leuven Junior Mobility Programme (JuMo).

K. Łukasik is with the Department of Electrical Engineering, KU Leuven, 3000 Leuven, Belgium. He is also with the Institute of Electronic Systems, Department of Electronics and Information Technology, Warsaw University of Technology, 00-665 Warsaw, Poland (e-mail: konstanty.lukasik@kuleuven.be, k.lukasik@stud.elka.pw.edu.pl).

J. Cheron and D. F. Williams are with the National Institute of Standards and Technology, Boulder, CO 80305, USA.

G. Avolio was with the Department of Electrical Engineering, KU Leuven, 3000 Leuven. He is now with Anteverta-mw B.V., 5656 AE Eindhoven, The Netherlands.

A. Lewandowski and W. Wiatr are with Institute of Electronic Systems, Department of Electronics and Information Technology, Warsaw University of Technology, 00-665 Warsaw, Poland.

D. M. M.-P. Schreurs is with the Department of Electrical Engineering, KU Leuven, 3000 Leuven.

Work partially supported by US government, not protected by US copyright.

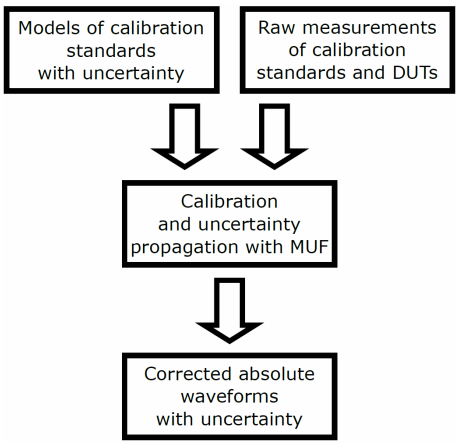

Fig. 1. Calibration procedure when using the MUF [16]

cable bending, coaxial connector repeatability [21], probe alignment, and even random errors [22] in our analysis. It is, however, worth noting that the MUF is not the only software package that can be used for estimating uncertainty in microwave measurements [23].

Despite so many error sources contributing to the uncertainty in large-signal measurements, including uncertainties due to the harmonic phase reference (HPR) remains the most challenging task. The HPR is used for re-establishing phase relationships between waves measured at harmonically related frequencies. Its characterization relies on a multi-step procedure. First, an impulse response of a photodiode is measured with an electrooptic sampling system [24]. Then, this device is used to determine the impulse response of a sampling scope [25] with mismatch correction applied [26]. Finally, characterization of the HPR must be performed [27] [28]. Hence, performing a full procedure is very cumbersome and requires highly qualified personnel and, to the best knowledge of the authors, NIST is the only research institute that has harmonic phase references characterized with correlated uncertainty as a measurement service.

Knowing the uncertainty in the HPR's output signal, it is possible to perform an uncertainty analysis of large-signal measurements. It is important to stress that we do not actually measure the uncertainties. They are estimated based on the characteristics of the calibration standards. To do so, measurements of calibration standards along with their statistical models must be processed by the MUF, see Fig. 1. Thanks to such an approach, all the predefined error sources, such as those listed above, are propagated through the large-signal calibration procedure. As a result, we receive calibration coefficients identified with perfect calibration standards as well as the range within which we could expect the coefficients if the definitions of the standards are imperfect. We can investigate how the error sources impact the calibration by performing either a sensitivity or a Monte Carlo analysis. The former investigates how each error source individually affects the final correction terms while the latter considers all the errors simultaneously and perturbs the calibration coefficients accordingly. Finally, the coefficients are used to correct the raw DUT measurements and identify their ideal and error-perturbed values. An analogous procedure also applies to small-signal measurements.

Even though methods for computing uncertainty in large-signal measurements have already been established, there has been no thorough uncertainty analysis of frequency-domain waves and how it translates to uncertainty of figures of merit derived with these results. Moreover, how the uncertainty in those waves are affected by changing load conditions has not been examined. Such a procedure is performed in this paper.

In this paper, we employed the NIST MUF to perform sensitivity analysis and compute relevant uncertainty quantities. We chose this approach instead of the Monte Carlo simulations since the latter does not let us investigate the impact of the individual error sources on the final uncertainty results. Using typical notation for a two-port device, we define a_1 and b_1 as incident and scattered complex frequency-domain traveling voltage waves at port 1, while a_2 and b_2 are incident and scattered waves, respectively, at port 2. Since the port 2 waves are directly affected by changing load conditions, they are the focus of this section. We can compute the wave's covariance matrix, which gives us uncertainty of real and imaginary parts as well as the correlation between them. The waves are assumed to be linear combinations of n error sources, which we consider in our uncertainty analysis. For example, the b_2 wave at the given frequency can be expressed as:

$$b_2 = f(\xi_1, \xi_2, \ldots, \xi_n), \tag{1}$$

where variables ξ_n stand for error sources that can be traced to real variables, like the length of a calibration standard. The function f propagates all n errors through the large-signal calibration and gives a complex value of b_2.

All the physical error mechanisms may be grouped as an error vector Ξ. By assumption, they are uncorrelated to each other [12] and thus, their covariance matrix is diagonal:

$$\Sigma_\Xi = \begin{bmatrix} \sigma^2_{\xi_1} & & \\ & \ddots & \\ & & \sigma^2_{\xi_n} \end{bmatrix}. \tag{2}$$

The next step is calculating a Jacobian that provides us with information on how the wave responds to the individual error sources. For the purpose of this article, we separate how the errors affect real and imaginary parts of the waves. In the case of the b_2 wave, we define its Jacobian J_{b_2} as:

$$J_{b_2} = \begin{bmatrix} \frac{\partial \Re(b_2)}{\partial \xi_1} & \cdots & \frac{\partial \Re(b_2)}{\partial \xi_n} \\ \frac{\partial \Im(b_2)}{\partial \xi_1} & \cdots & \frac{\partial \Im(b_2)}{\partial \xi_n} \end{bmatrix}. \tag{3}$$

Knowing the error vector's covariance matrix Σ_Ξ and the wave's Jacobian J_{b_2}, we can compute covariance matrix of the b_2 wave:

$$\Sigma_{b_2} = J_{b_2} \cdot \Sigma_\Xi \cdot J^T_{b_2}, \tag{4}$$

which can be defined as:

$$\Sigma_{b_2} = \begin{bmatrix} \sigma^2_{\Re(b_2)} & \sigma_{\Re(b_2)\Im(b_2)} \\ \sigma_{\Re(b_2)\Im(b_2)} & \sigma^2_{\Im(b_2)} \end{bmatrix}, \tag{5}$$

where the diagonal terms are variances of the wave's real and imaginary parts while $\sigma_{\Re(b_2)\Im(b_2)}$ stands for covariance between them.

Therefore, $\sigma_{\Re(b_2)\Im(b_2)}$ provides us with the variance of the b_2's real and imaginary parts as well as their dependence on each other. Using Σ_{b_2}, it is possible to derive additional quantities. We define the total variance of b_2 as:

$$\sigma_{b_2}^2 = \lambda_1 + \lambda_2, \tag{6}$$

where λ_1 and λ_2 are eigenvalues of the b_2's covariance matrix. $\sigma_{b_2}^2$ could simply be interpreted as a sum of the real and imaginary components, however, (6) allows to account for $\sigma_{\Re(b_2)\Im(b_2)}$ as well. Having identified the covariance matrix, it's also possible to compute uncertainty of the b_2's magnitude

$$|b_2| = \sqrt{\Re(b_2)^2 + \Im(b_2)^2}. \tag{7}$$

Any change of $|b_2|$ caused by shifts in $\Re(b_2)$ and $\Im(b_2)$ can be expressed as

$$d|b_2| = \frac{\partial|b_2|}{\partial\Re(b_2)} d\Re(b_2) + \frac{\partial|b_2|}{\partial\Im(b_2)} d\Im(b_2), \tag{8}$$

where the derivatives can be calculated in terms of:

$$\frac{\partial|b_2|}{\partial\Re(b_2)} = \frac{\Re(b_2)}{|b_2|}, \tag{9}$$

$$\frac{\partial|b_2|}{\partial\Im(b_2)} = \frac{\Im(b_2)}{|b_2|}. \tag{10}$$

The variance of $|b_2|$ can be computed as the expected value of the change in the b_2's magnitude squared

$$\sigma_{|b_2|}^2 = E\left((d|b_2|)^2\right). \tag{11}$$

Variations of $\Re(b_2)$ and $\Im(b_2)$ resulting in $d|b_2|$ are substituted by standard deviations of the b_2's real and imaginary parts, in which the covariance matrix Σ_{b_2} [1,2] also appears. The result is

$$\begin{aligned}\sigma_{|b_2|}^2 \quad = \quad & \left(\tfrac{\partial|b_2|}{\partial\Re(b_2)}\right)^2 \cdot \sigma_{\Re(b_2)}^2 + \\ & \left(\tfrac{\partial|b_2|}{\partial\Im(b_2)}\right)^2 \cdot \sigma_{\Im(b_2)}^2 + \\ & 2 \cdot \tfrac{\partial|b_2|}{\partial\Re(b_2)} \cdot \tfrac{\partial|b_2|}{\partial\Im(b_2)} \cdot \sigma_{\Re(b_2)\Im(b_2)}.\end{aligned} \tag{12}$$

Subsequently, the uncertainty of the b_2's phase is derived. We can compute $\phi(b_2)$ with the following equation

$$\phi(b_2) = \arctan\left(\frac{\Im(b_2)}{\Re(b_2)}\right). \tag{13}$$

First, its change with regards to the varying $\Re(b_2)$ and $\Im(b_2)$ is

$$d\phi(b_2) = \frac{\partial\phi(b_2)}{\partial\Re(b_2)} d\Re(b_2) + \frac{\partial\phi(b_2)}{\partial\Im(b_2)} d\Im(b_2). \tag{14}$$

Computing partial derivatives of $\phi(b_2)$, we obtain

$$\frac{\partial\phi(b_2)}{\partial\Re(b_2)} = \frac{1}{1+\left(\frac{\Im(b_2)}{\Re(b_2)}\right)^2} \cdot \frac{-\Im(b_2)}{\Re(b_2)^2}, \tag{15}$$

$$\frac{\partial\phi(b_2)}{\partial\Im(b_2)} = \frac{1}{1+\left(\frac{\Im(b_2)}{\Re(b_2)}\right)^2} \cdot \frac{1}{\Re(b_2)}. \tag{16}$$

Finally, we can calculate the variance of the b_2's phase as

$$\sigma_{\phi(b_2)}^2 = E\left((d\phi(b_2))^2\right) \tag{17}$$

When we expand the equation and consider the covariance between the real and imaginary parts of the b_2 wave, we obtain

$$\begin{aligned}\sigma_{\phi(b_2)}^2 \quad = \quad & \left(\tfrac{\partial\phi(b_2)}{\partial\Re(b_2)}\right)^2 \cdot \sigma_{\Re(b_2)}^2 + \\ & \left(\tfrac{\partial\phi(b_2)}{\partial\Im(b_2)}\right)^2 \cdot \sigma_{\Im(b_2)}^2 + \\ & 2 \cdot \tfrac{\partial\phi(b_2)}{\partial\Re(b_2)} \cdot \tfrac{\partial\phi(b_2)}{\partial\Im(b_2)} \cdot \sigma_{\Re(b_2)\Im(b_2)}.\end{aligned} \tag{18}$$

$\sigma_{a_2}^2$, $\sigma_{|a_2|}^2$, and $\sigma_{\phi(a_2)}^2$ are calculated similarly. In the next sections, standard deviations will be used for discussing the uncertainty in the experiments performed.

Knowing the uncertainty in b_2 and a_2, it is possible to investigate how their uncertainty affects figures of merit that represent the performance of microwave devices. As an example, we can derive uncertainty of the power delivered to the load P_{out} as

$$P_{out} = \frac{|b_2|^2 - |a_2|^2}{2Z_0}. \tag{19}$$

Since $|b_2|$ and $|a_2|$ directly affect P_{out}, they also define its uncertainty. To identify $\sigma_{P_{out}}$, we use an equation for computing the standard deviation of a generic parameter y dependent on N variables x [29]

$$\sigma_y = \sqrt{\sum_{i=1}^{N}\sum_{j=1}^{N} \frac{\partial f}{\partial x_i}\frac{\partial f}{\partial x_j}\sigma_{x_i x_j}}, \tag{20}$$

which can be further simplified if we assume the variables x are uncorrelated:

$$\sigma_y = \sqrt{\sum_{i=1}^{N}\left(\frac{\partial f}{\partial x_i}\right)^2 \sigma_{x_i}^2}. \tag{21}$$

Since this assumption is valid for magnitudes of the b_2 and a_2 waves [17], we derive the standard deviation of P_{out} as:

$$\sigma_{P_{out}} = \sqrt{\left(\frac{\partial P_{out}}{\partial|b_2|}\right)^2 \cdot \sigma_{|b_2|}^2 + \left(\frac{\partial P_{out}}{\partial|a_2|}\right)^2 \cdot \sigma_{|a_2|}^2}, \tag{22}$$

which simplified takes a form of

$$\sigma_{P_{out}} = \frac{\sqrt{|b_2|\cdot\sigma_{|b_2|}^2 + |a_2|\cdot\sigma_{|a_2|}^2}}{Z_0}. \tag{23}$$

This method of computing $\sigma_{P_{out}}$ is a simplification. A Monte-Carlo approach can be used, but then it is not possible to track sources of error in the problem. Reference [29] suggests higher-order terms in the Taylor series expansion

should be included if the function is highly nonlinear. But even with this approach, tracking error sources will be imperfect due to the interaction of errors in the nonlinear function. In the case considered, it means a device generating non-negligible amount of power at higher harmonics. Nevertheless, the definition of the output power's standard deviation provided in (23) is sufficient to give microwave designers indication whether their circuit will conform to the design requirements. Furthermore, such an approach allows us to easily compare our results with relevant publications, like reference [17] that implies the uncertainty of P_{out} increases with the magnitude of the load reflection coefficient Γ_L for all its phases.

III. Load-Pull Measurement System

In this section, we present the set up used for performing load-pull measurements. The schematic diagram is shown in Fig. 2. A nonlinear vector network analyzer (NVNA) measured frequency-domain waves directly at the device's terminals. To achieve this on the DUT's output and avoid de-embedding of the passive tuner, we used a set of external couplers connected directly to the NVNA's receivers. In the figure, they are denoted as the output port reflectometer. An internal bias-tee of the network analyzer was used to set the DC voltage at the DUT's input. On the output side, an external bias-tee was located outside the passive tuner.

A mixer-based Keysight LSNA, PNA-X N5245A[1], operating in the frequency range up to 50 GHz, was used for the large-signal measurements. The external output reflectometer consisted of two low-loss directional Marki CA-50[1] couplers and was connected to the output probe with a short cable. HP 4142B modular DC supplies[1] were used for setting the requested bias voltages at the input and output terminals of the DUT.

For the load-pull measurements, we used a Focus Microwave MPT-1818[1] passive tuner, which is capable of tuning up to three harmonics at frequencies between 1.8 and 18 GHz. However, we only used it to set load reflection coefficient at the fundamental frequency. We characterized the instrument with the manufacturer's software [30]. This is achieved by measuring the tuner's S-parameters in multiple tuning states. To ensure that the characterization procedure is valid, the measurements of the instrument must be very accurate. Thus, the NVNA was calibrated with the unknown *thru* scheme [31] due to its high accuracy. Gathered data and the reflection coefficient of the tuner's termination are used by the control software to accurately set Γ_T at the tuner's input. However, if reflection coefficients other than those used as the characterization tuning states are needed, interpolation methods are employed. However, any inaccuracies due to the operation of the tuning method can be ignored because the NVNA measures absolute waves and thus, we exactly know what reflection coefficient has been achieved.

Since the passive tuner is connected to the DUT through the output reflectometer, we needed to consider its characteristics

[1]Trade names are used here only to fully specify the experimental configuration and do not constitute an endorsement by NIST. Other instruments made by the same or different manufacturer may function as well or better for this application.

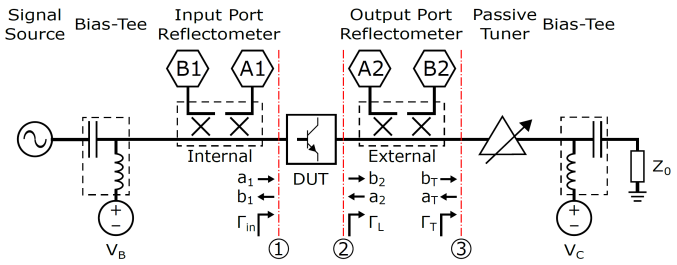

Fig. 2. Block diagram of a passive load-pull system used for experiments. A1, B1, A2, and B2 denote the internal receivers of the NVNA that measure the frequency-domain waves a_1, b_1, a_2, and b_2, respectively

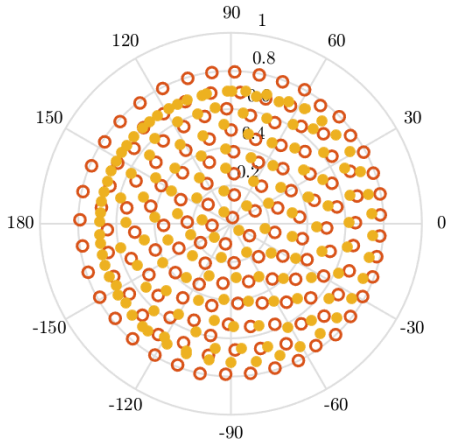

Fig. 3. Load reflection coefficients Γ_L identified by CVT (red circles) and measured (orange dots) at $f_0 = 9$ GHz during experiments, $P_{av} = 0$ dBm

while calculating Γ_T so as to provide the requested load reflection coefficient Γ_L at the output of the DUT, see Fig. 2. Due to this configuration, the reflectometer's losses limit the maximum $|\Gamma_L|$. Knowing the maximum magnitude of the reflection coefficient achievable by the tuner, which is around 0.92, as well as the total insertion loss of the external couplers and the on-wafer fixture, we decided to limit $|\Gamma_L|$ to 0.8. Values of Γ_L to be measured were identified with Centroidal Voronoi Tessellation (CVT) [32] [33], which is a space division method that, in our case, ensures a uniform coverage of the Smith chart. Target load reflection coefficients are marked as orange dots in Fig. 3. For our experiments, we employed CVT to define 149 load reflection coefficients. This number of loads was chosen as a trade-off between the highly dense coverage of the Smith chart and the total measurement time.

Using the setup described, we performed large-signal measurements of state-of-the-art indium phosphide (InP) heterojunction bipolar transistors (HBTs) manufactured by Teledyne Technologies[1] [34]. Their emitter is 250 nm wide. For our experiments, we used the transistors with 6 μm long emitter. They were biased to achieve the collector current $I_C = 6$ mA at the collector voltage $V_C = 1.5$ V. This operating point was chosen to achieve high power gain when used in a power amplifier configuration at mmWave frequencies. Complex waves at four harmonics were measured with the fundamental frequency $f_0 = 9$ GHz. Available input power P_{av} was set between -30 and 0 dBm. The reflection coefficient Γ_L was varied at f_0

Table I
SOLT CALIBRATION STANDARDS WITH ASSOCIATED STANDRD UNCERTAINTIES

General Characteristics	
Inner conductor diameter (mm)	1.042±0.004
Outer conductor diameter (mm)	2.400±0.005
Pin diameter (mm)	0.511±0.005
Offset Short and Open	
Line length (mm)	6.750±0.005
Offset Load	
Line length (mm)	7.700±0.005
Load resistance (Ω)	50.0±0.7
Load inductance (nH)	0.02±0.02

Table II
TRL CALIBRATION STANDARDS WITH ASSOCIATED STANDARD UNCERTAINTIES. PARAMETERS L AND W ARE THE TRANSMISSION LINE'S LENGTH AND WIDTH, RESPECTIVELY. H IS THE SUBSTRATE'S THICKNESS

	Line 1	Line 2	Line 3
L (μm)	290±0.05	774±0.05	2000±0.05
W (μm)	11.6±0.05		
H (μm)	5±0.5		

Table III
NOMINAL PHASES OF THE COMB GENERATOR ALONG WITH THEIR STANDARD UNCERTAINTIES

Frequency (GHz)	9	18	27	36
Phase (°)	169.5±0.5	160.2±0.6	152.0±0.9	148.2±1.0

over the points defined in the previous paragraph. Measured Γ_L, shown as orange dots in Fig. 3, is calculated using the following equation:

$$\Gamma_L = \frac{a_{2,nom}}{b_{2,nom}}, \tag{24}$$

where $a_{2,nom}$ and $b_{2,nom}$ are a frequency waves at the fundamental frequency f_0 corrected with the nominal MUF calibration unperturbed by any simulated error sources. Despite limiting the magnitude of the load reflection coefficient, we observe that the measured Γ_L constellation is further compressed and off-center. It is particularly noticeable on the left side of the plot, for $\phi(\Gamma_L)$ from to 90° or -90° where $|\Gamma_L|$ hardly reaches 0.7. On the opposite side, the magnitudes go up to 0.75. This shift may be attributed to the characterization of the tuner's termination, which consisted of a bias-tee and a 50 Ω load. Whereas the additional decrease of $|\Gamma_L|$ is probably a result of the extra loss introduced by the short transmission lines connecting the transistors to the probe pads or our overestimation how high the magnitude of the tuner's reflection coefficient Γ_T at f_0 may be achieved. The load impedance at the second harmonic $2f_0$ was set to 50 Ω. Effectively, the magnitude of Γ_L at $2f_0$ was within 0.3 while its phase varied. These load conditions can impact the uncertainty in the waves at the second harmonic. However, the correlation between frequency-domain waves at different frequencies was confirmed to be negligible. Therefore, the uncertainty in the waves at $2f_0$ does not affect the results gathered at f_0.

Since the load-pull experiments were done on-wafer, a two-tier calibration procedure was executed. First, a Short-Open-Load-Thru (SOLT) [35] coaxial large-signal calibration was accomplished. Then, the NVNA was connected to the probe station and an on-wafer multiline Thru-Reflect-Line (TRL) [36] [37] calibration was performed such that the reference planes could be moved to the device terminals. Therefore, both coaxial SOLT and on-wafer TRL standards had to be provided with uncertainty resulting from their imperfect physical parameters. TRL standards were manufactured on the same substrate as the DUTs. Raw measurements of all calibration standards, including the HPR and the power meter, were taken. They were used for performing an on-wafer large-signal calibration with the NIST MUF, as defined by a simplified flow chart shown in Fig. 1. Resultant correction coefficients were applied to uncalibrated measurements of the transistor.

All the error sources considered were propagated through the calibration procedure. Physical parameters and the associated standard uncertainties of the SOLT and TRL calibration artifacts are listed in Table I and II, respectively. The length of the on-wafer thru and reflect artifacts is 0. Moreover, models of the TRL standards include the repeatability of the probe positioning. The uncertainty of the left-to-right alignment is equal to ±20 μm. For including the possible cable bending errors, we took measurements of a thru on-wafer standard while changing the position of the cable. Furthermore, Tab. III reports the phases of the NIST-characterized comb generator [27] [28] along with their standard uncertainties at the frequencies relevant for the calibration procedure. Next, we accounted for the errors in the power meter measurements based on [38]. They stem from the reference oscillator mismatch, the reference oscillator power uncertainty, the zero-set error, the zero carry-over error, the instrumentation error, and error in the power sensor calibration factor. Finally, the HPR's and power meter's reflection coefficients were considered as well.

IV. UNCERTAINTY IN FREQUENCY-DOMAIN WAVES UNDER SMALL-SIGNAL CONDITIONS

Knowing how the measurements were performed, we can finally report results of frequency waves uncertainty analysis. First, we estimate the uncertainty in frequency-domain waves when the transistor operates under a small-signal regime, that is at $P_{av} = -22$ dBm. σ_{b_2}, see Fig. 4, increases particularly quickly when $\phi(\Gamma_L)$ is around 30°. The b_2 standard deviation increases significantly slower outside this area of the load reflection coefficient and the lowest rate is when $\phi(\Gamma_L)$ approaches -150°.

Fig. 5a shows how the magnitude of the b_2 wave is dependent on the changing reflection coefficient Γ_L. It achieves its maximum value when the magnitude of the reflection coefficient is high and its phase nears 35°. This is in line with our expectations where the InP transistors used for the experiments should achieve the highest magnitude of their output signal. Consequently, $|b_2|$ steadily decreases towards the opposite side of the plot where $\phi(\Gamma_L)$ approaches -145°. The wave's standard deviation $\sigma(|b_2|)$, presented in Fig. 5b, acts similarly and has its maximum in the same region as the

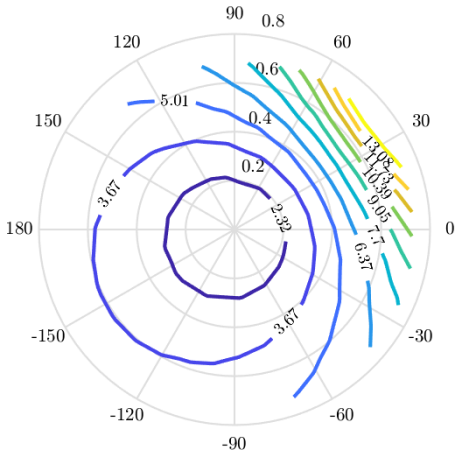

Fig. 4. Standard deviation of the b_2 wave, σ_{b_2} (mV), at f_0 in relation to Γ_L, $P_{av} = -22$ dBm

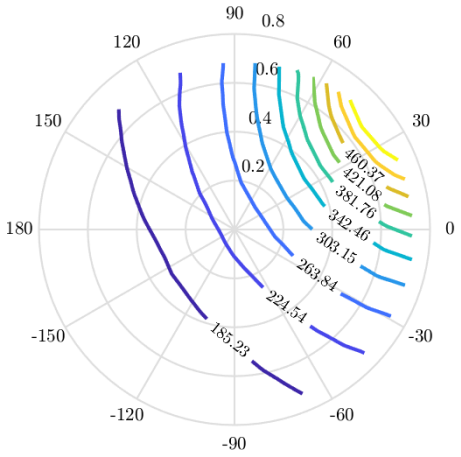

(a) $|b_2|$ (mV)

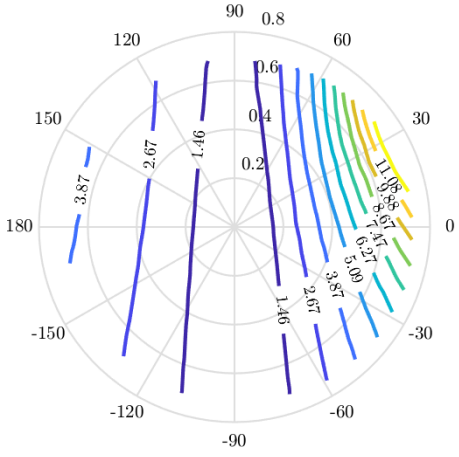

(b) $\sigma_{|b_2|}$ (mV)

Fig. 5. (a) Magnitude of b_2 and (b) its standard deviation at f_0 in relation to Γ_L, $P_{av} = -22$ dBm

$|b_2|$ wave. When $\phi(\Gamma_L)$ is close to 90° or -90°, the standard deviation of b_2's magnitude is low. However, the magnitude's uncertainty slightly increases when $\phi(\Gamma_L)$ is close to 180° and $|\Gamma_L|$ raises.

Considering the b_2 wave's phase, shown in Fig. 6a, we

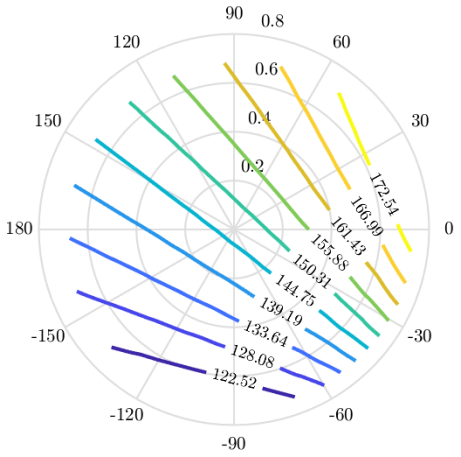

(a) $\phi(b_2)$ (°)

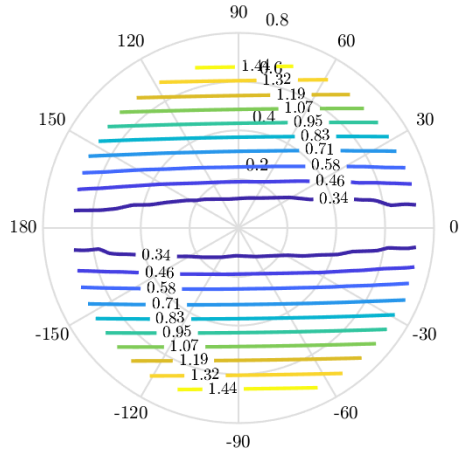

(b) $\sigma_{\phi(b_2)}$ (°)

Fig. 6. (a) Phase of b_2 and (b) its standard deviation at f_0 in relation to Γ_L, $P_{av} = -22$ dBm

observe that it gradually increases from the bottom towards the top right quarter of the plot. The standard deviation of the b_2's phase, which is shown in Fig. 6b, rises towards the bottom and the top of the plot along the y-axis. While the load reflection coefficient's phase is around 0° and 180° degrees, $\sigma_{\phi(b_2)}$ is practically unrelated to the Γ_L's magnitude. Furthermore, $\sigma_{\phi(b_2)}$'s dependence on Γ_L practically rotates by 90° when compared with $\sigma(|b_2|)$.

The b_2 wave's dependence on $|\Gamma_L|$ and $\phi(\Gamma_L)$ can be described as orthogonal and thus results in what is shown in Fig. 4. Therefore, even though we might at first have assumed that the standard deviation of the b_2 is solely related to Γ_L's magnitude, the actual dependence of b_2 on the load reflection coefficient is more complex and both the magnitude and phase of Γ_L have to be considered.

When analyzing the standard deviation of the a_2 wave, shown in Fig. 7, it clearly increases when $\phi(\Gamma_L)$ is close to 35° and $|\Gamma_L|$ is high.σ_{a_2} decreases towards the opposite end of the plot, that is where $\phi(\Gamma_L)$ is close to -150° and $|\Gamma_L|$ is high. The behavior of σ_{a_2} is similar to σ_{b_2}, shown in Fig. 4. However, it's more concentrated around its maximum. Another noteworthy observation is the similarity between the σ_{a_2}'s contours and the behavior of the b_2's magnitude, which can be seen in Fig.

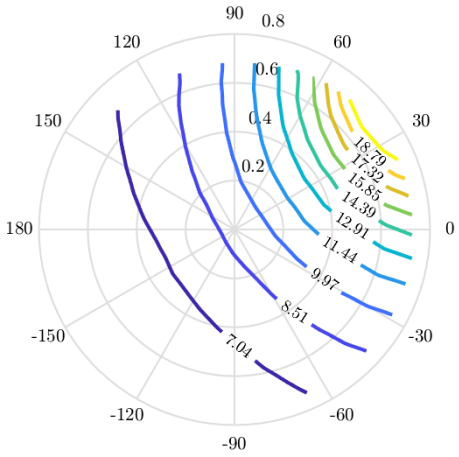

Fig. 7. Standard deviation of the a_2 wave, σ_{a_2} (mV), at f_0 in relation to Γ_L, $P_{av} = -22$ dBm

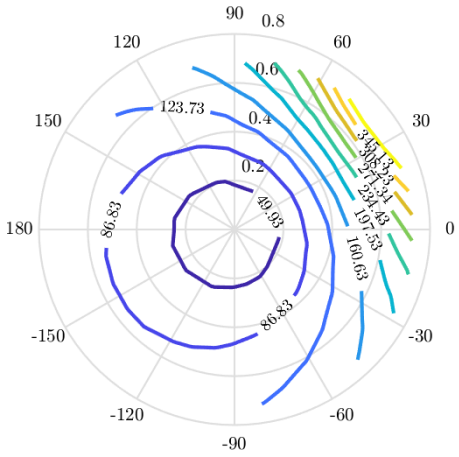

(a) $|a_2|$ (mV)

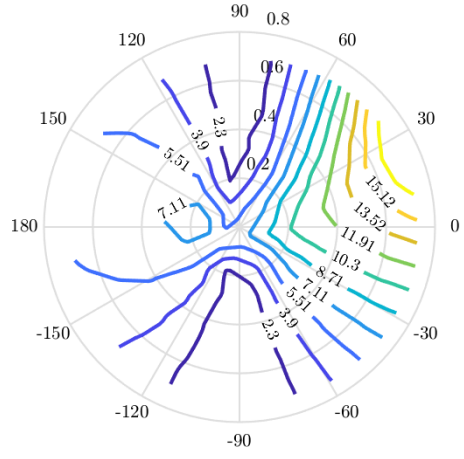

(b) $\sigma_{|a_2|}$ (mV)

Fig. 8. (a) Magnitude of a_2 and (b) its standard deviation at f_0 in relation to Γ_L, $P_{av} = -22$ dBm

5a. Additionally, σ_{a_2} is higher than σ_{b_2}.

As expected, the magnitude of a_2, which is shown in Fig. 8a, follows $|b_2|$. However, its contours are very similar to the plot of σ_{b_2} from Fig. 4. Consequently, $\sigma_{|a_2|}$, see Fig. 8b, also follows the b_2 wave and is largest when the phase of the load

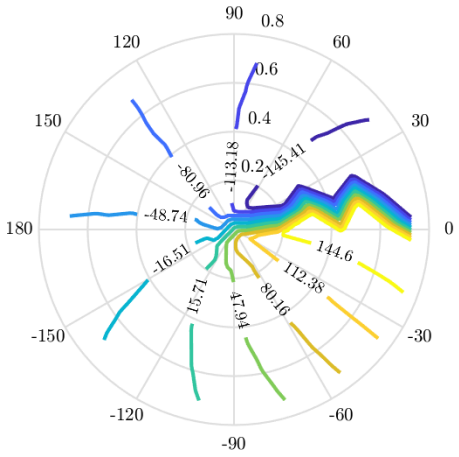

(a) $\phi(a_2)$ (°)

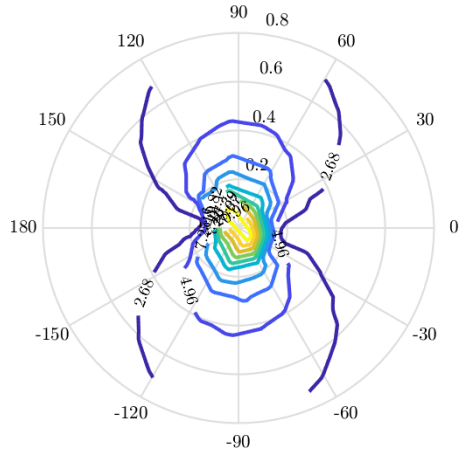

(b) $\sigma_{\phi(a_2)}$ (°)

Fig. 9. (a) Phase of a_2 and (b) its standard deviation at f_0 in relation to Γ_L, $P_{av} = -22$ dBm

reflection coefficient is close to 25° and the magnitude of Γ_L is around 0.7, just like $\sigma_{|b_2|}$. When $\phi(\Gamma_L)$ is close to 90° and -90°, $\sigma_{|a_2|}$ is small and further decreases when $|\Gamma_L|$ rises. As $\phi(\Gamma_L)$ nears 180°, $\sigma_{|a_2|}$ slightly increases. On top of this, we observe that $\sigma_{|a_2|}$ is generally higher than $\sigma_{|b_2|}$ at this input power level.

We also investigated the phase of the a_2 wave, which is presented in Fig. 9a. Subsequently, Fig. 9b shows the standard deviation of $\phi(a_2)$, which is largest when the magnitude of Γ_L is small and rapidly decreases when it gets higher. The decrease rate is higher along the x-axis, that is when $\phi(\Gamma_L)$ close to 0° or 180°. We suspect that the uncertainty of the a_2's phase is highest in the middle of the plot due to low levels of $|a_2|$. This makes the measurements of a_2 more susceptible to noise and other error sources. Thus, even slight changes of the real or imaginary parts of a_2 can cause high variability of $\sigma_{\phi(a_2)}$.

Knowing the a_2 and b_2 waves and uncertainty of their magnitudes, it is possible to compute the device's output power P_{out} delivered to the load, see (19). Fig. 10a shows how P_{out} behaves when the reflection coefficient Γ_L changes. P_{out} achieves its maximum when $|\Gamma_L|$ is about 0.7 while $\phi(\Gamma_L)$ is close to 35°. For other reflection coefficients, P_{out} steadily

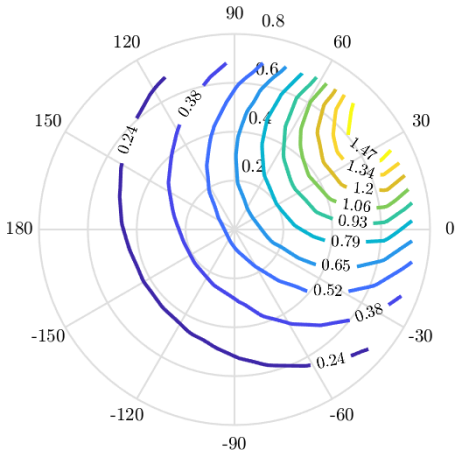

(a) P_{out} (mW)

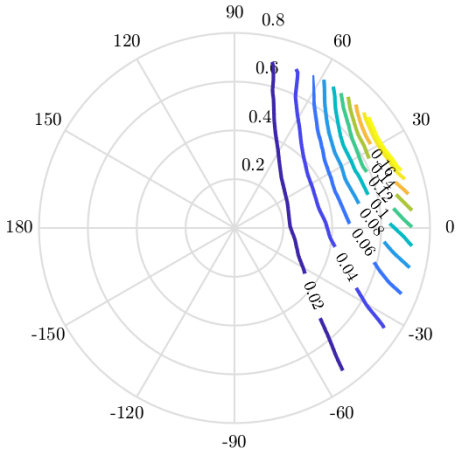

(b) $\sigma_{P_{out}}$ (mW)

Fig. 10. (a) Output power P_{out} and its (b) standard deviation at f_0 in relation to Γ_L, $P_{av} = -22$ dBm

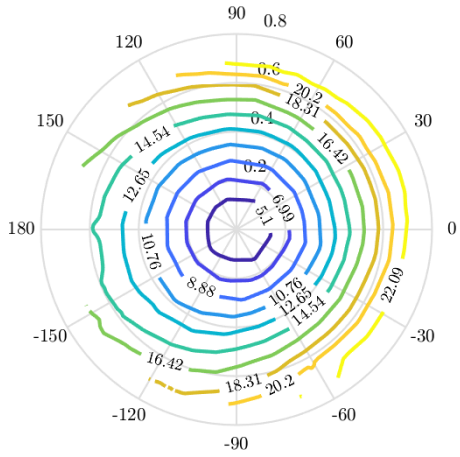

Fig. 11. Standard deviation of b_2, σ_{b_2} (mV), at f_0 in relation to Γ_L, $P_{av} = 0$ dBm

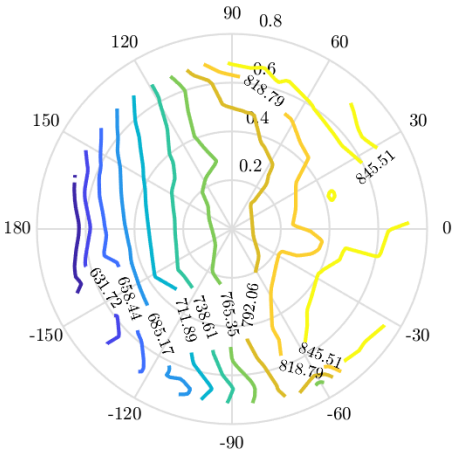

(a) $|b_2|$ (mV)

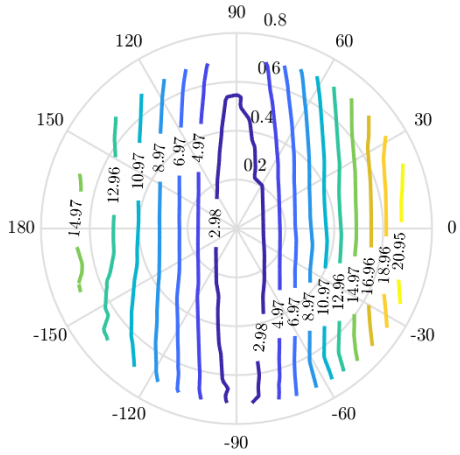

(b) $\sigma_{|b_2|}$ (mV)

Fig. 12. (a) Magnitude of b_2 and (b) its standard deviation at f_0 in relation to Γ_L, $P_{av} = 0$ dBm

decreases. As expected, the output power closely follows the magnitude characteristics of the b_2 and a_2 waves shown in Fig. 5a and 8a, respectively.

If we consider the standard deviation of P_{out}, shown in Fig. 10b, we see that it reaches its maximum when $|\Gamma_L|$ is around 0.7 and $\phi(\Gamma_L)$ reaches 30°. Such a behavior could be expected based on plots of $\sigma_{|b_2|}$ and $\sigma_{|a_2|}$, see Fig. 5b and 8b.

V. Uncertainty in Frequency-Domain Waves Under Large-Signal Conditions

Considering the device's behavior under large-signal conditions, at $P_{av} = 0$ dBm, we observe very similar results to what was shown for the transistor working in the small-signal regime, that is at $P_{av} = -22$ dBm. Looking at Fig. 11, we could conclude that the standard deviation of the b_2 wave is simply proportional to the magnitude of the load reflection coefficient Γ_L while virtually independent of its phase. However, to completely understand this, it is necessary to analyze how the uncertainty of b_2's magnitude and phase behave in relation to the changing load.

Starting with the characteristic of the b_2's magnitude, see Fig. 12a, we observe that it steadily rises along the x-axis towards the *open* side of the plot, that is when $\phi(\Gamma_L)$ close to 0° and $|\Gamma_L|$ approaches 0.7. Next, Fig. 12b shows the standard deviation of the wave's magnitude $\sigma_{|b_2|}$, which increases with Γ_L's magnitude but only when the phase of the reflection coefficient is close to 0° or 180°. The rate of the change is significantly higher in the right part of the plot. This aligns

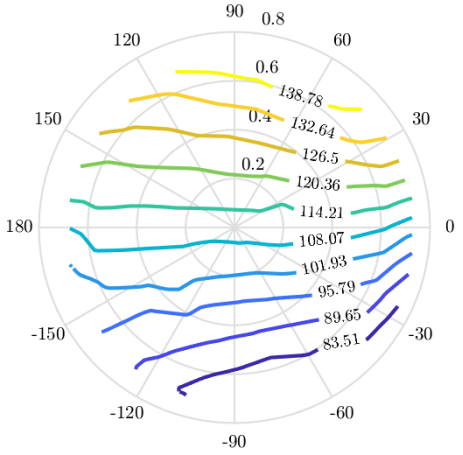

(a) $\phi(b_2)$ (°)

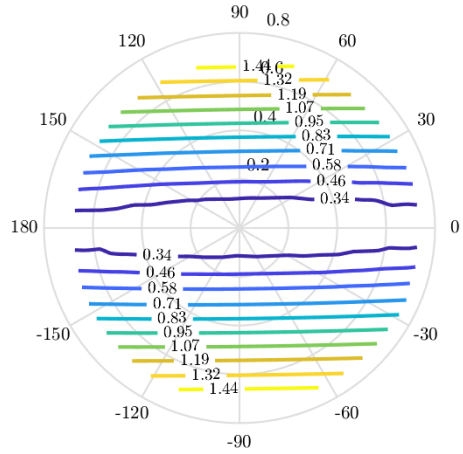

(b) $\sigma_{\phi(b_2)}$ (°)

Fig. 13. (a) Phase of b_2 and (b) its standard deviation at f_0 in relation to Γ_L, $P_{av} = 0$ dBm

with the behavior of $|b_2|$. When the Γ_L's phase gets close to 90° or -90°, $\sigma_{|b_2|}$ is practically independent of $|\Gamma_L|$. Finally, it's noteworthy that $\sigma_{|b_2|}$ acts similarly to its counterpart measured at $P_{av} = -22$ dBm.

The phase of the b_2 wave was investigated as well. Its graph is shown in Fig. 13a. It is highest as $\phi(\Gamma_L)$ approaches 75° and $|\Gamma_L|$ is high. Its lowest values are observed when $\phi(\Gamma_L)$ is close to -60°. However, considering the standard deviation of the b_2's phase, shown in Fig. 13b, it is particularly noteworthy the characteristic of $\sigma_{\phi(b_2)}$ is virtually identical to the characteristic of this parameter at $P_{av} = -22$ dBm, see Fig. 6b, with just insignificant value differences.

Analyzing the a_2 wave's uncertainty, sweeping the reflection coefficient over the specified area does not cause significant changes in the a_2's standard deviation, shown in Fig. 14. Moreover, those changes are relatively smaller than in the case of the small-signal conditions, see Fig. 7. Nevertheless, σ_{a_2} steadily increases as Γ_L approaches open circuit conditions. Finally, the uncertainty of a_2 closely follows the characteristic of the b_2's magnitude, which is shown in Fig. 12b. Thus, the σ_{a_2}'s behavior under large-signal conditions is in line with its small-signal counterpart.

In Fig. 15a, we show the magnitude of a_2 under changing

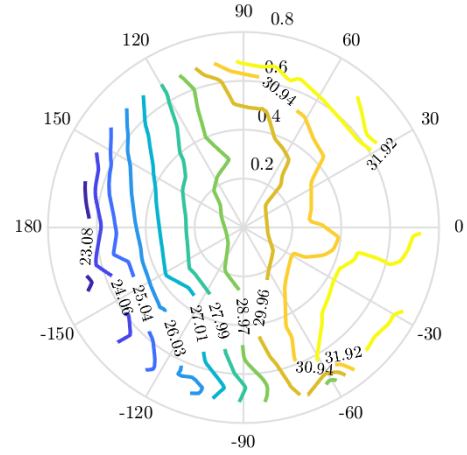

Fig. 14. Standard deviation of a_2, σ_{a_2} (mV), at f_0 in relation to Γ_L, $P_{av} = 0$ dBm

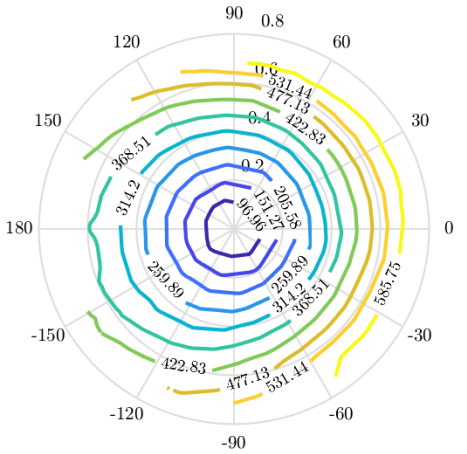

(a) $|a_2|$ (mV)

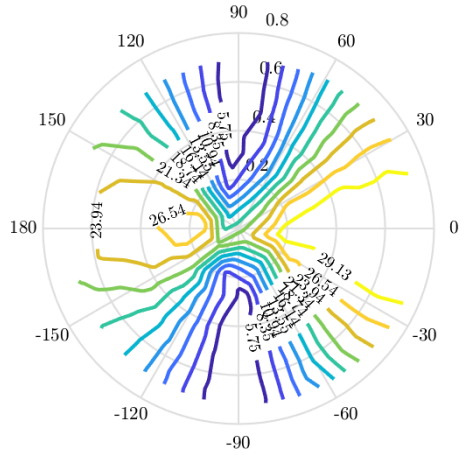

(b) $\sigma_{|a_2|}$ (mV)

Fig. 15. (a) Magnitude of a_2 and (b) its standard deviation at f_0 in relation to Γ_L, $P_{av} = 0$ dBm

load conditions. As expected, $|a_2|$ rises when $|\Gamma_L|$'s nears the maximum values achievable by the measurement setup. $|a_2|$ at $P_{av} = 0$ dBm acts similarly to this wave's magnitude under small-signal conditions and thus, its contours are almost identical to σ_{b_2} in Fig. 11. The standard deviation of $|a_2|$, see

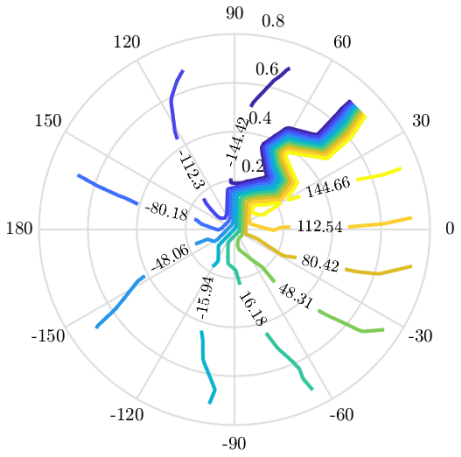

(a) $\phi(a_2)$ (°)

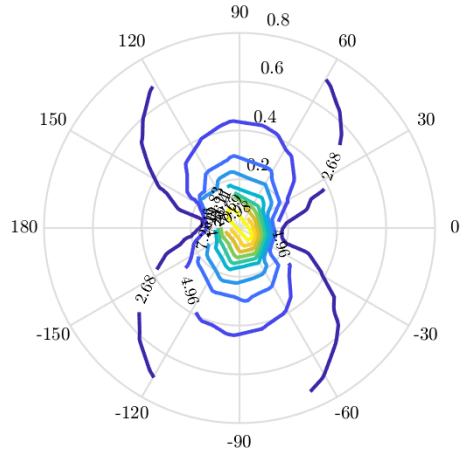

(b) $\sigma_{\phi(a_2)}$ (°)

Fig. 16. (a) Phase of a_2 and (b) its standard deviation at f_0 in relation to Γ_L, $P_{av} = 0$ dBm

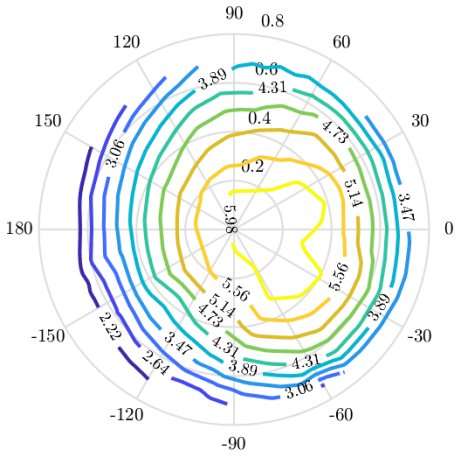

(a) P_{out} (mW)

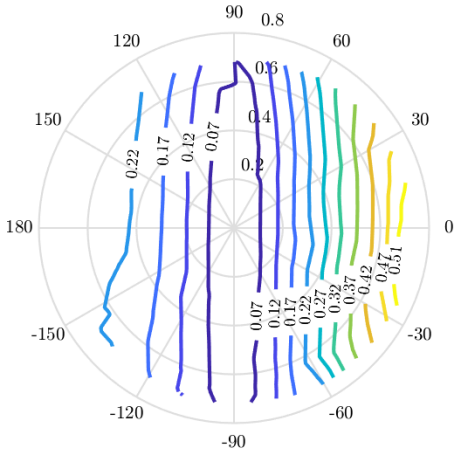

(b) $\sigma_{P_{out}}$ (mW)

Fig. 17. (a) Output power P_{out} and its (b) standard deviation at f_0 in relation to Γ_L, $P_{av} = 0$ dBm

Fig. 15b, achieves its maximum in the same region as $\sigma_{|b_2|}$ from Fig. 12b. $\sigma_{|a_2|}$ increases noticeably faster when $\phi(\Gamma_L)$ is close to 180° in comparison to its small-signal counterpart in Fig. 8b. As before, $\sigma_{|a_2|}$ is higher than $\sigma_{|b_2|}$ at the same power level.

Fig. 16a shows the phase of a_2 under large-signal conditions. Just like b_2 at $P_{av} = 0$ dBm, $\sigma_{\phi(a_2)}$ has a very similar behavior to its counterpart when the DUT is excited with the small signal, see Fig. 16b and 9b, respectively.

As in the case of measurement under small-signal conditions, we can analyze P_{out} and it standard deviation. For $P_{av} = 0$ dBm, we observe the maximum output power is achieved when $|\Gamma_L|$ is 0.2 and $\phi(\Gamma_L)$ equal to around 0°, see Fig. 17a. This is a significant change in comparison with the P_{out}'s behavior at $P_{av} = -22$ dBm, shown in Fig. 10a.

$\sigma_{P_{out}}$, see Fig. 17b, follows this change as it is highest when the phase of the reflection coefficient gets close to 0° and its magnitude is high. As in the small-signal case, this behavior could be expected if the uncertainty in the b_2 and a_2 waves's magnitudes are scrutinized, see Fig. 12b and 12b, respectively.

Figures of $\sigma_{P_{out}}$ for two operation conditions undeniably show that when considering uncertainty of the device's figures of merit under changing load conditions, we need to analyze them in relation to both the magnitude and the phase of the load reflection coefficient. Otherwise, we lose important dependencies that may invalidate the design process.

VI. Juxtaposition of Small- and Large-Signal Conditions

For comparison, uncertainty in the DUT's b_2 wave at two power levels, that is $P_{av} = -22$ dBm and $P_{av} = 0$ dBm, are displayed in the same figures. Fig. 18a presents standard deviation of the b_2 wave with regards to the magnitude of the reflection coefficient. As already suggested by analyzing Fig. 11 and 4, there is seemingly a clear correlation between σ_{b_2} and $|\Gamma_L|$.

However, this assumption is invalidated by Fig. 18b, which shows dependence of $\sigma_{|b_2|}$ on $|\Gamma_L|$. This plot shows that $\sigma_{|b_2|}$ is not necessarily high when the magnitude of Γ_L increases. Moreover, Fig. 19a clearly shows that the standard deviation of b_2's magnitude is strongly dependent on the phase of Γ_L. In Fig. 18a, we also observe the standard deviation of the b_2 wave increases when the input power level rises. The same applies to $\sigma_{|b_2|}$, based on Fig. 18b and 19a.

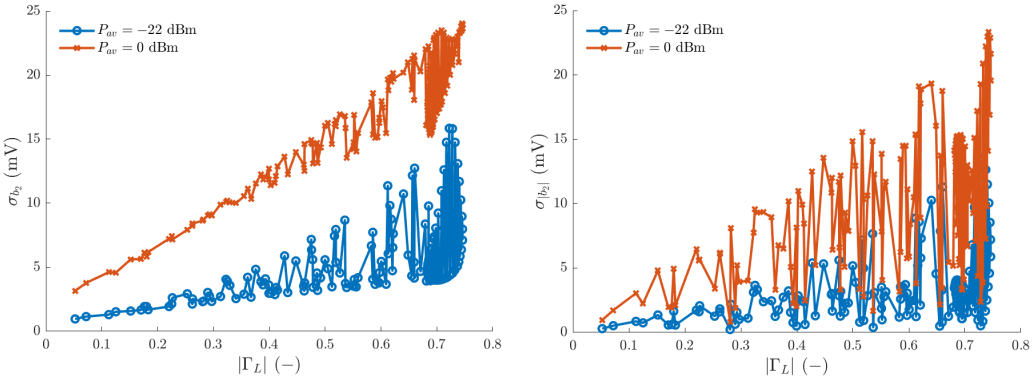

(a) σ_{b_2} (mV) (b) $\sigma_{|b_2|}$ (mV)

Fig. 18. Standard deviation of (a) b_2 and its (b) magnitude in relation to $|\Gamma_L|$, for $-180° < \phi(\Gamma_L) < 180°$

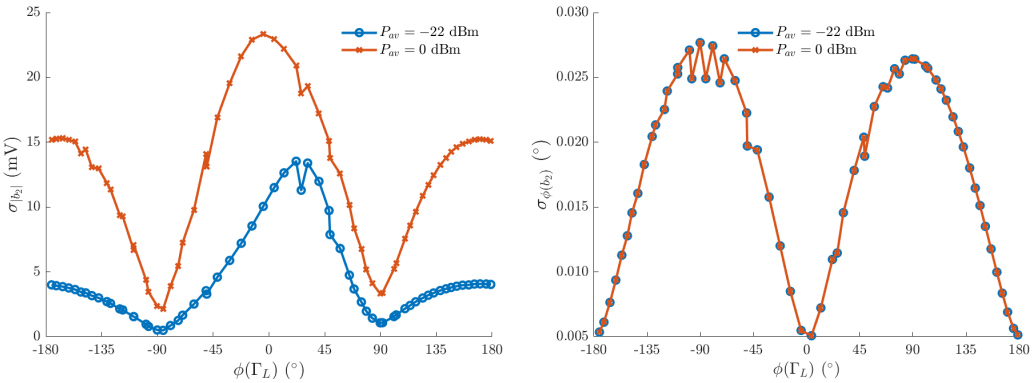

(a) $\sigma_{|b_2|}$ (mV) (b) $\sigma_{\phi(b_2)}$ (°)

Fig. 19. Standard deviation of b_2's (a) magnitude and (b) phase at f_0 in relation to $\phi(\Gamma_L)$, for $|\Gamma_L| \geq 0.65$

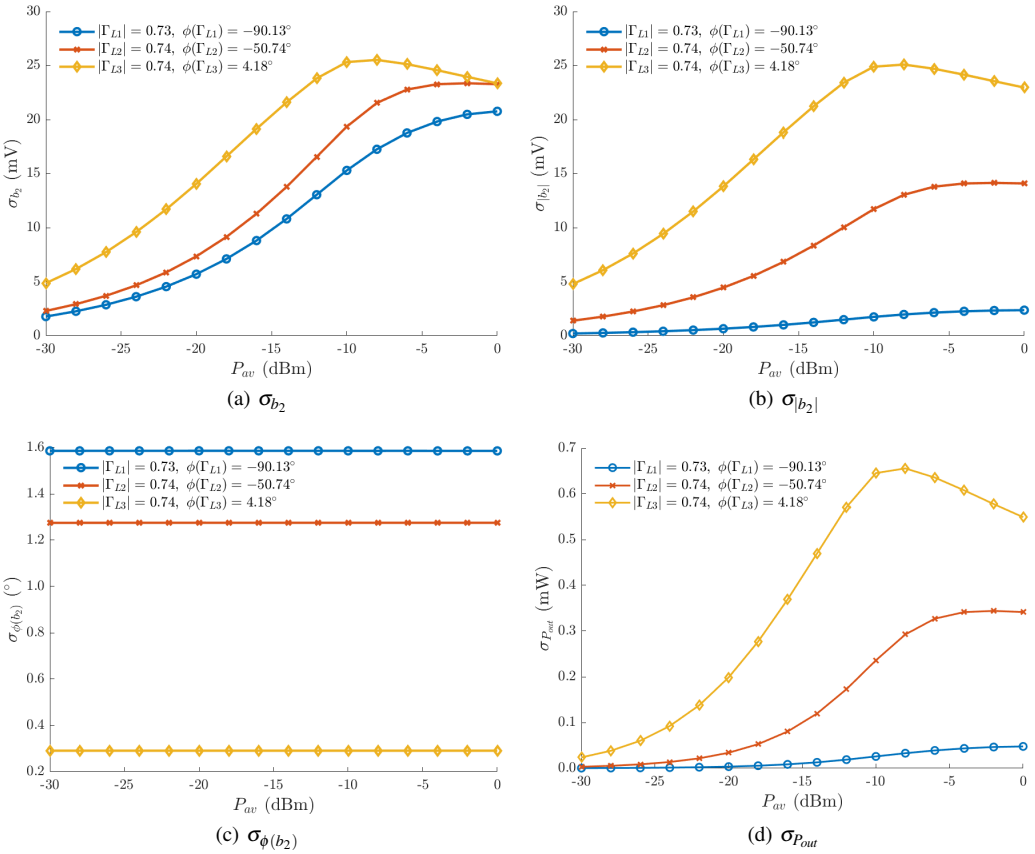

(a) σ_{b_2} (b) $\sigma_{|b_2|}$

(c) $\sigma_{\phi(b_2)}$ (d) $\sigma_{P_{out}}$

Fig. 20. Standard deviation of (a) b_2, its (b) magnitude and (c) phase at f_0 as well as (d) P_{out} in relation to P_{av}

Table IV
TOTAL AND INDIVIDUAL UNCERTAINTY CONTRIBUTIONS IN THE MAGNITUDE AND PHASE OF THE b_2 WAVE UNDER THREE DISTINCT LOAD CONDITIONS FOR $P_{av} = 0$ dBm

	$\lvert\Gamma_{L1}\rvert = 0.73,\ \phi(\Gamma_{L1}) = -90.13°$		$\lvert\Gamma_{L2}\rvert = 0.74,\ \phi(\Gamma_{L2}) = -50.74°$		$\lvert\Gamma_{L3}\rvert = 0.74,\ \phi(\Gamma_{L3}) = 4.18°$	
	$\sigma_{\lvert b_2\rvert}$ (mV)	$\sigma_{\phi(b_2)}$ (°)	$\sigma_{\lvert b_2\rvert}$ (mV)	$\sigma_{\phi(b_2)}$ (°)	$\sigma_{\lvert b_2\rvert}$ (mV)	$\sigma_{\phi(b_2)}$ (°)
Total	2.467	1.584	13.938	1.291	22.963	0.291
TRL	1.731	1.559	13.696	1.270	22.896	0.133
SOLT	1.176	0.144	1.414	0.139	1.181	0.151
Power Meter	0.133	0.006	0.169	0.002	0.058	0.011
Comb Generator Repeatability	$5.904 \cdot 10^{-12}$	$2.054 \cdot 10^{-13}$	$7.045 \cdot 10^{-12}$	$2.943 \cdot 10^{-13}$	$5.218 \cdot 10^{-12}$	$3.484 \cdot 10^{-13}$
Comb Generator Characterization	$9.965 \cdot 10^{-11}$	$3.407 \cdot 10^{-12}$	$1.151 \cdot 10^{-10}$	$3.941 \cdot 10^{-12}$	$8.988 \cdot 10^{-11}$	$4.768 \cdot 10^{-12}$
Probe Alignment	0.756	0.173	0.743	0.179	0.394	0.184
Cable Bending	0.073	0.005	0.079	0.006	0.082	0.005

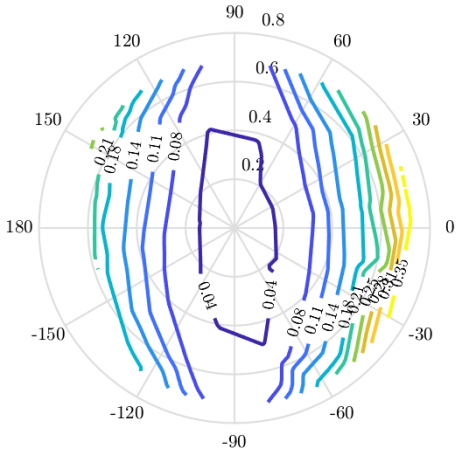

Fig. 21. Standard deviation of the output power P_{out} for a slice of P_{out} between 2.1 and 2.3 mW

On top of this, $\sigma_{\phi(b_2)}$ also has a strong dependence on $\phi(\Gamma_L)$ as displayed in Fig. 19b that confirms conclusions reached analyzing Fig. 13b and 6b. Since both traces practically overlap, Fig. 19b also confirms that the phase error only slightly changes when the input power is increased.

Finally, it is worth showing how these parameters behave over the entire sweep of the input power level at three illustrative reflection coefficients. Under these load conditions summarized in Tab. IV, three distinct cases can be identified:

1) At Γ_{L1}, σ_{b_2} is predominantly a result of $\sigma_{\phi(b_2)}$,
2) At Γ_{L2}, σ_{b_2} is a result of both $\sigma_{|b_2|}$ and $\sigma_{\phi(b_2)}$,
3) At Γ_{L3}, σ_{b_2} is mainly a result of $\sigma_{|b_2|}$.

As shown in Fig. 20a, σ_{b_2} increases with the input power level P_{av}. This agrees with the results shown by previous paragraphs of this section. The behavior of $\sigma_{|b_2|}$, see Fig. 20b, is also in line with our expectations, thus, it's largest when $\phi(\Gamma_L)$ is close to 0°. Then, $\sigma_{|b_2|}$ decreases when $\phi(\Gamma_L)$ approaches -90°. $\sigma_{\phi(b_2)}$ also acts as anticipated and we do not see significant variations of this parameters while increasing P_{av} for the particular Γ_L. As before, we observe that $\sigma_{\phi(b_2)}$ is smallest when $\phi(\Gamma_L)$ is around 0° while $\sigma_{\phi(b_2)}$ reaches its peak when $\phi(\Gamma_L)$ equals to around -90°.

As expected considering the results shown in the previous sections, Fig. 20d shows that the standard deviation of P_{out} closely follows the uncertainty of b_2's magnitude. Thus, $\sigma_{P_{out}}$, just like $\sigma_{|b_2|}$, is dependent on both $|\Gamma_L|$ and $\phi(\Gamma_L)$.

Furthermore, by limiting the range of the output power P_{out}, we make its uncertainty analysis independent of large P_{out} changes over the whole Smith chart. In Fig. 21, we chose the P_{out} slice that is within the maximum $\sigma_{P_{out}}$ but gives us enough measurement points for interpolation. Thus, we set the P_{out} range between 2.1 and 2.4 mW and identified 79 load points across input available powers P_{av} ranging from -20 to 0 dBm. Despite the limited P_{out} range, $\sigma_{P_{out}}$ still closely follows the general behavior of uncertainty of the b_2 and a_2 waves' magnitudes, that is it increases towards the areas where $|\Gamma_L|$ is high and $\phi(\Gamma_L)$) is close to 0 or 180°. Thus, it may be concluded that the behavior of $\sigma_{P_{out}}$ is independent of the P_{out} values.

It's also worth analyzing how the main uncertainty sources, delineated in Sec. III, contribute to the uncertainty of the b_2 wave's magnitude and phase. In Tab. IV, we present the individual deviations when the DUT operates at $P_{av} = 0$ dBm and under the three distinct load conditions already discussed in this section. In all the cases considered, the main causes of the uncertainty are the TRL and SOLT vector calibrations. Moreover, the TRL correction procedure's contribution to $\sigma_{|b_2|}$ rapidly increases when $\phi(\Gamma_L)$ gets close to 0°. In the case of $\sigma_{\phi(b_2)}$, the behavior is opposite. Thus, the behavior of $\sigma_{\phi(b_2)}$ shown in Fig. 9b and 16b may be attributed to the TRL calibration scheme. Individual deviations due the SOLT calibration do not change with the varying load conditions. The errors originating from the probe alignment are also significant. The power meter measurements and the cable bending have small but definitely non-negligible contributions. Whereas, the inaccuracy caused by the characterization and repeatability of the HPR can practically be ignored.

VII. SUMMARY OF THE RESULTS

Considering the results shown in the previous subsections, we can sum up the behavior of the b_2 wave's uncertainties:

1) $\sigma_{|b_2|}$ rapidly increases when Γ_L approaches the optimum load. Regardless of this, when $\phi(\Gamma_L)$ is close to 90° or -90°, $\sigma_{|b_2|}$ is low and practically independent of $|\Gamma_L|$,

2) $\sigma_{\phi(b_2)}$ is only directly dependent on $|\Gamma_L|$ when $\phi(\Gamma_L)$ is close to 90° or -90°. When $\phi(\Gamma_L)$ is close to 0° or 180°, $\sigma_{|b_2|}$ is low and practically independent of $|\Gamma_L|$,
3) Behavior of σ_{b_2} is a result of the first two dependencies – this parameter increases with $|\Gamma_L|$ for all $\phi(\Gamma_L)$,
4) σ_{b_2} and $\sigma_{|b_2|}$ are proportional to the P_{av} level,
5) $\sigma_{\phi(b_2)}$ is virtually independent of the P_{av} levels.

Referring to the uncertainty in the a_2 wave, we have the following inferences for the test case considered here:

1) $\sigma_{|a_2|}$ closely follows $\sigma_{|b_2|}$ and thus, increases as Γ_L gets close to the optimum load. However, $\sigma_{|a_2|}$ is higher than $\sigma_{|b_2|}$ at all the input power levels P_{av},
2) $\sigma_{\phi(a_2)}$ is in inverse proportion to $|\Gamma_L|$. $\sigma_{\phi(a_2)}$ decreases more rapidly when $\phi(\Gamma_L)$ is close to 0° or 180°,
3) σ_{a_2} has similar characteristic to the magnitude of b_2 and as well achieves its maximum when Γ_L gets close to the optimum load. Furthermore, σ_{a_2} is higher than σ_{b_2},
4) σ_{a_2} and $\sigma_{|a_2|}$ are proportional to the P_{av} level,
5) $\sigma_{\phi(a_2)}$ is stable at all the P_{av} levels.

We assume that those findings are applicable also to devices other than the InP HBTs we used for performing the experiments. Furthermore, the dependencies of the b_2 and a_2 waves on the load reflection coefficient also affect figures of merit. By calculating the standard deviation of P_{out}, we have proven it's not only related to the the magnitude of the reflection coefficient, like in [17], but to its phase as well.

All the results presented in the paper may be of great value to the designers of microwave circuits. The knowledge of uncertainty in load-pull measurements could be used for extracting and validating nonlinear transistor models within a range of confidence [39]. Either using such models or measurement results directly, the designers can guarantee that circuits comply with the design requirements even in the worst-case scenarios [11]. If we could provide load-pull uncertainty data in real-time, another application could be adaptive sampling for modeling purposes [40]. In this case, the information provided by the uncertainty data could be used for safely choosing subsequent measurement points without violating the DUT's operational constraints [41]. Unfortunately, existing measurement platforms cannot provide real-time uncertainty in nonlinear measurements.

VIII. Conclusion

In this paper, we evaluated uncertainty in large signal measurements under changing load conditions. In contrast to other relevant publications, we focused on frequency waves and investigated their residual errors. We included multiple sources of uncertainties in our analysis, such as passive calibration standards, power meter, NIST traceable phase calibration reference, and cable bending. For this purpose, we performed on-wafer load-pull measurements of the InP HBT transistors. Then, we were able to estimate the uncertainties in the frequency-domain waves by using the NIST Microwave Uncertainty Framework.

Since b_2 and a_2 are directly influenced by changing load conditions, we focused on their standard deviations of these waves as well as their magnitudes and phases. b_2 is particularly interesting as its uncertainty is dependent on both the phase and magnitude of Γ_L. We observe this behavior due to orthogonality of $\sigma_{|b_2|}$ and $\sigma_{\phi(b_2)}$ in relation to Γ_L. Interestingly, σ_{a_2} closely follows the magnitude of the b_2's magnitude. Another noteworthy observation is that neither $\sigma_{\phi(b_2)}$ nor $\sigma_{\phi(a_2)}$ increases with the input power level even though standard deviations of these waves, as well as their magnitudes, rise when more power is delivered to the DUT. On top of this, uncertainties related to the a_2 wave and its magnitude are higher than those affecting b_2.

In the paper, we also show the uncertainty of output power P_{out}, that is the power delivered to the load. This figure of merit illustrates how the uncertainty of performance quantities may be indirectly dependent on both the magnitude and phase of the load reflection coefficient. Thus, those relationships need to be considered during the development process if such performance figures are employed to design microwave circuits.

References

[1] A. Ferrero and M. Pirola, "Harmonic load-pull techniques: An overview of modern systems," *IEEE Microw. Mag.*, vol. 14, no. 4, pp. 116–123, June 2013.
[2] J. Verspecht, "Large-signal network analysis," *IEEE Microw. Mag.*, vol. 6, no. 4, pp. 82–92, Dec. 2005.
[3] W. V. Moer and L. Gomme, "NVNA versus LSNA: enemies or friends?" *IEEE Trans. Microw. Theory Techn.*, vol. 11, no. 1, pp. 97–103, Feb. 2010.
[4] F. M. Ghannouchi, R. Larose, R. G. Bosisio, and Y. Demers, "A six-port network analyzer load-pull system for active load tuning," *IEEE Trans. Instrum. Meas.*, vol. 39, no. 4, pp. 628–631, Aug. 1990.
[5] M. S. Hashmi, A. L. Clarke, S. P. Woodington, J. Lees, J. Benedikt, and P. J. Tasker, "An accurate calibrate-able multiharmonic active load-pull system based on the envelope load-pull concept," *IEEE Trans. Microw. Theory Techn.*, vol. 58, no. 3, pp. 656–664, Mar. 2010.
[6] F. M. Ghannouchi, M. S. Hashmi, S. Bensmida, and M. Helaoui, "Loop enhanced passive source- and load-pull technique for high reflection factor synthesis," *IEEE Trans. Microw. Theory Techn.*, vol. 58, no. 11, pp. 2952–2959, Nov. 2010.
[7] M. Marchetti, M. J. Pelk, K. Buisman, W. C. E. Neo, M. Spirito, and L. C. N. de Vreede, "Active harmonic load-pull with realistic wideband communications signals," *IEEE Trans. Microw. Theory Techn.*, vol. 56, no. 12, pp. 2979–2988, Dec. 2008.
[8] P. Barmuta, F. Ferranti, G. P. Gibiino, A. Lewandowski, and D. M. M.-P. Schreurs, "Compact Behavioral Models of Nonlinear Active Devices Using Response Surface Methodology," *IEEE Trans. Microw. Theory Techn.*, vol. 63, no. 1, pp. 56–64, Jan. 2015.
[9] J. Cheron, D. F. Williams, K. Łukasik, R. A. Chamberlin, B. F. Jamroz, E. N. Grossman, W. Wiatr, and D. Schreurs, "Propagation of compact-modeling measurement uncertainty to 220 GHz power-amplifier designs," in *2018 Asia-Pacific Microw. Conf. (APMC)*, Nov. 2018, pp. 744–746.
[10] X. Cui, S. J. Doo, P. Roblin, J. Strahler, and R. G. Rojas-Teran, "High efficiency RF power amplifier designed with harmonic real-time active load-pull," *IEEE Microw. Wireless Compon. Lett.*, vol. 18, no. 4, pp. 266–268, Apr. 2008.
[11] D. F. Williams, R. A. Chamberlin, W. Zhao, J. Cheron, and M. E. Urteaga, "The Role of Measurement Uncertainty in Achieving First-Pass Design Success," in *2016 IEEE Comp. Semicond. Int. Circ. Symp. (CSICS)*, Oct. 2016, pp. 1–4.
[12] A. Lewandowski, D. F. Williams, P. D. Hale, J. C. M. Wang, and A. Dienstfrey, "Covariance-based vector-network-analyzer uncertainty analysis for time- and frequency-domain measurements," *IEEE Trans. Microw. Theory Techn.*, vol. 58, no. 7, pp. 1877–1886, July 2010.
[13] V. Teppati and A. Ferrero, "A comparison of uncertainty evaluation methods for on-wafer S-parameter measurements," *IEEE Trans. Instrum. Meas.*, vol. 63, no. 4, pp. 935–942, Apr. 2014.

[14] M. Garelli and A. Ferrero, "A unified theory for S-parameter uncertainty evaluation," *IEEE Trans. Microw. Theory Techn.*, vol. 60, no. 12, pp. 3844–3855, Dec. 2012.
[15] M. Wollensack, J. Hoffmann, J. Ruefenacht, and M. Zeier, "VNA Tools II: S-parameter uncertainty calculation," in *2012 7th ARFTG Microw. Meas. Conf.*, June 2012, pp. 1–5.
[16] G. Avolio, A. Raffo, J. Jargon, P. D. Hale, D. M. M.-P. Schreurs, and D. F. Williams, "Evaluation of uncertainty in temporal waveforms of microwave transistors," *IEEE Trans. Microw. Theory Techn.*, vol. 63, no. 7, pp. 2353–2363, July 2015.
[17] A. Ferrero, V. Teppati, and A. Carullo, "Accuracy evaluation of on-wafer load-pull measurements," *IEEE Trans. Microw. Theory Techn.*, vol. 49, no. 1, pp. 39–43, Jan. 2001.
[18] V. Teppati and C. R. Bolognesi, "Evaluation and reduction of calibration residual uncertainty in load-pull measurements at millimeter-wave frequencies," *IEEE Trans. Microw. Theory Techn.*, vol. 61, no. 3, pp. 817–822, Mar. 2012.
[19] D. F. Williams, "NIST Microwave Uncertainty Framework," https://www.nist.gov/services-resources/software/wafer-calibration-software.
[20] H. C. Reader, D. F. Williams, P. D. Hale, and T. S. Clement, "Comb-Generator Characterization," *IEEE Trans. Microw. Theory Techn.*, vol. 56, no. 2, pp. 515–521, Feb. 2008.
[21] A. Lewandowski and D. F. Williams, "Stochastic modeling of coaxial-connector repeatability errors," in *2009 74th ARFTG Microw. Meas. Conf.*, Nov. 2009, pp. 1–4.
[22] A. Lewandowski and D. Williams, "Characterization and modeling of random vector network analyzer measurement errors," in *2008 Int. Conf. Microw. Radar and Wireless Comm. (MIKON)*, May 2008, pp. 1–4.
[23] G. Avolio, D. F. Williams, S. Streett, M. Frey, D. Schreurs, A. Ferrero, and M. Dieudonné, "Software tools for uncertainty evaluation in VNA measurements: A comparative study," in *2017 89th ARFTG Microw. Meas. Conf.*, June 2017, pp. 1–7.
[24] D. F. Williams, A. Lewandowski, T. S. Clement, J. C. M. Wang, P. D. Hale, J. M. Morgan, D. A. Keenan, and A. Dienstfrey, "Covariance-based uncertainty analysis of the NIST electrooptic sampling system," *IEEE Trans. Microw. Theory Techn.*, vol. 54, no. 1, pp. 481–491, Jan. 2006.
[25] T. S. Clement, P. D. Hale, D. F. Williams, C. M. Wang, A. Dienstfrey, and D. A. Keenan, "Calibration of sampling oscilloscopes with high-speed photodiodes," *IEEE Trans. Microw. Theory Techn.*, vol. 54, no. 8, pp. 3173–3181, Aug. 2006.
[26] D. F. Williams, T. S. Clement, P. D. Hale, and A. Dienstfrey, "Terminology for high-speed sampling-oscilloscope calibration," in *2006 68th ARFTG Microw. Meas. Conf.*, Nov. 2006, pp. 1–6.
[27] H. C. Reader, D. F. Williams, P. D. Hale, and T. S. Clement, "Comb-Generator Characterization," *IEEE Trans. Microw. Theory Techn.*, vol. 56, no. 2, pp. 515–521, Feb. 2008.
[28] P. D. Hale, A. Dienstfrey, J. C. M. Wang, D. F. Williams, A. Lewandowski, D. A. Keenan, and T. S. Clement, "Traceable waveform calibration with a covariance-based uncertainty analysis," *IEEE Trans. Instrum. Meas.*, vol. 58, no. 10, pp. 3554–3568, Oct. 2009.
[29] "Evaluation of measurement data - Guide to the expression of uncertainty in measurement," Joint Committee for Guides in Metrology (JCGM), Tech. Rep., 1995.
[30] "Focus Microwave Device Characterization Suite," https://focus-microwaves.com/wp-content/uploads/2018/05/Product-Brochure_FDCS_Focus-Microwaves-Group_2018.pdf.
[31] A. Ferrero and U. Pisani, "Two-port network analyzer calibration using an unknown 'thru'," *IEEE Microw. Guided Wave Lett.*, vol. 2, no. 12, pp. 505–507, Dec. 1992.
[32] P. Barmuta, G. P. Gibiino, F. Ferranti, A. Lewandowski, and D. M. M.-P. Schreurs, "Design of Experiments Using Centroidal Voronoi Tessellation," *IEEE Trans. Microw. Theory Techn.*, vol. 64, no. 11, Nov. 2016.
[33] P. Barmuta, K. Łukasik, F. Ferranti, G. P. Gibiino, A. Lewandowski, and D. Schreurs, "Load-pull measurements using Centroidal Voronoi Tessellation," in *2017 89th ARFTG Microw. Meas. Conf.*, June 2017, pp. 1–4.
[34] Z. Griffith, M. Urteaga, P. Rowell, R. Pierson, and M. Field, "Multi-finger 250nm InP HBTs for 220 GHz mm-wave power," in *2012 Int. Conf. on Indium Phosphide and Rel. Mat.*, Aug. 2012, pp. 204–207.
[35] R. A. Ginley, "Establishing traceability for SOLT calibration kits," in *2017 90th ARFTG Microw. Meas. Conf.*, Nov. 2017, pp. 1–4.
[36] R. Marks, "A multiline method of network analyzer calibration," *IEEE Trans. Microw. Theory Techn.*, vol. 39, no. 7, pp. 1205–1215, July 1991.
[37] D. F. Williams, J. C. M. Wang, and U. Arz, "An optimal vector-network-analyzer calibration algorithm," *IEEE Trans. Microw. Theory Techn.*, vol. 51, no. 12, pp. 2391–2401, Dec. 2003.
[38] *Fundamentals of RF and Microwave Power Measurements (Part 3)*, Keysight Technologies, Santa Rosa, CA, 2014, Appl. Note AN 1449-3.
[39] D. F. Williams, R. A. Chamberlin, W. Zhao, J. Cheron, and M. E. Urteaga, "Transistor Model Verification Including Measurement Uncertainty," *IEEE Trans. Microw. Theory Techn.*, vol. 64, no. 11, pp. 3927–3933, Nov. 2016.
[40] P. Barmuta, G. Avolio, F. Ferranti, A. Lewandowski, L. Knockaert, and D. M. M.-P. Schreurs, "Hybrid Nonlinear Modeling Using Adaptive Sampling," *IEEE Trans. Microw. Theory Techn.*, vol. 63, no. 12, pp. 4501–4510, Dec. 2015.
[41] P. Barmuta, F. Ferranti, A. Lewandowski, and D. M. M.-P. Schreurs, "Dynamic Constraints for Large-Signal Measurements on Arbitrary Grids," *IEEE Trans. Microw. Theory Techn.*, vol. 64, no. 11, pp. 3956–3964, Nov. 2016.

Konstanty Łukasik received the B.Sc. and M.Sc. degrees in electrical engineering from the Warsaw University of Technology, Poland, in 2014 and 2015, respectively. He is currently pursuing a dual-degree Ph.D. at KU Leuven, Belgium, and the Warsaw University of Technology. In 2017, he was a Guest Researcher with the National Institute of Standards and Technology, Boulder, CO, USA. Since 2017, he has also been collaborating with Keysight Technologies, Santa Rosa, CA, USA. His current research interests include microwave measurements, transistor and PA modeling, design of experiments, as well as measurement uncertainty analysis.

Jerome Cheron received the Ph.D. degree in electrical engineering from the University of Limoges, France, in 2011. He was involved in a research project with the XLIM Laboratory and Thales Air Systems. In 2012, he was a Post-Doctoral Fellow with the Fraunhofer IAF, Freiburg, Germany. In 2013, he joined the National Institute of Standards and Technology, Boulder, Colorado, USA. His current research interests include the modeling and design of millimeter-wave and terahertz active-circuits in III-V technology.

Gustavo Avolio was born in Cosenza, Italy, in 1982. He received the MSc. in electronic engineering from the University of Calabria, Italy, in 2006. In 2012 he obtained the PhD in electronic engineering from KU Leuven, Belgium. From 2012 till 2017 he was a post-doctoral researcher supported by FWO Vlaanderen Belgium. In 2013, 2014, and 2016 he has been a Visiting Scientist at the National Institute of Standards and Technology (NIST), Boulder, Colorado. He is now with Anteverta-mw/Maury Microwave (Netherlands), and his work focuses on large-signal measurements and modeling.

Arkadiusz Lewandowski (M'09) received the M.Sc. degree and the Ph.D degree (with honors) in electrical engineering from the Warsaw University of Technology, Poland, in 2001 and 2010, respectively.

He joined the Institute of Electronics Systems, Warsaw University of Technology, in 2002, where he conducts research in the area of microwave measurements. From 2002 to 2004 he was involved in the development of digital synthesizers of radar signals with the Telecommunications Research Institute, Warsaw, Poland. From 2004 to 2008 he has been a Guest Researcher at the National Institute of Standards and Technology, Boulder, USA. Since 2015 he has been collaborating with the Institute of Agrophysics, Polish Academy of Sciences, Lublin, Poland in the area of material measurements. He has authored and co-authored 24 journal papers and over 60 conference papers. His current research interests concern small- and large-signal microwave measurements, material measurements, and modeling of passive and active microwave devices.

Dylan F. Williams (M'80-SM'90-F'02) received a Ph.D. in Electrical Engineering from the University of California, Berkeley in 1986. He joined the Electromagnetic Fields Division of the National Institute of Standards and Technology in 1989 where he develops electrical waveform and microwave metrology. He has published over 100 technical papers and is a Fellow of the IEEE. He is the recipient of the Department of Commerce Bronze and Silver Medals, the Astin Measurement Science Award, two Electrical Engineering Laboratory's Outstanding Paper Awards, three Automatic RF Techniques Group (ARFTG) Best Paper Awards, the ARFTG Automated Measurements Technology Award, the IEEE Morris E. Leeds Award, the European Microwave Prize and the 2013 IEEE Joseph F. Keithley Award. Dylan also served as Editor of the IEEE Transactions on Microwave Theory and Techniques from 2006 to 2010, as the Executive Editor of the IEEE Transactions on Terahertz Science and Technology, and as the 2017 President of the IEEE Microwave Theory and Techniques Society.

Wojciech Wiatr (M'96) received the M.Sc., Ph.D., and D.Sc. degrees in electronics engineering from the Warsaw University of Technology, Warsaw, Poland, in 1970, 1980, and 2015, respectively. Since 1972, he has been with the Institute of Electronic Systems, Warsaw University of Technology, where he is currently a Professor Emeritus. He has been involved in new techniques and instrumentation for broadband scattering and noise parameter measurements of microwave transistors and monolithic microwave integrated circuits. He is an inventor of the RF multistate total power radiometer realizing simultaneous noise and vector analysis of microwave networks with natural noise excitation. In noise metrology, he collaborated with the National Radio Astronomy Observatory, Charlottesville, VA, USA, the Ferdinand-Braun-Institut fï¿œr Hï¿œchstfrequenztechnik, Berlin, Germany, and the National Institute of Standards and Technology, Boulder, CO, USA. He has authored or co-authored more than 90 papers and 1 book. He holds two patents. His current research interests include development of techniques for precision microwave measurements and materials characterization.

Dominique M. M.-P. Schreurs (S'90-M'97-SM'02-F'12) received the M.Sc. degree in electronic engineering and the Ph.D. degree from the University of Leuven (KU Leuven), Leuven, Belgium, in 1992 and 1997, respectively.

She has been a Visiting Scientist with Agilent Technologies, Santa Rosa, CA, USA, ETH Zurich, Zï¿œrich, Switzerland, and the National Institute of Standards and Technology, Boulder, CO, USA. She is currently a Full Professor with KU Leuven, where she is also the Chair of the Leuven LICT. Her current research interests include the microwave and millimeter-wave characterization and modeling of transistors, nonlinear circuits, and bioliquids, and system design for wireless communications and biomedical applications.

Prof. Schreurs served as President of the IEEE Microwave Theory and Techniques Society (April 2018-2019), and priorly was Editor-in-Chief of the IEEE Transactions on Microwave Theory and Techniques as well as IEEE MTT-S Distinguished Microwave Lecturer. She also served as President of the ARFTG organization (2018-2019) and was General Chair of the 2007, 2012, and 2018 Spring ARFTG Conferences. In 2020, she serves as TPC chair of the European Microwave Conference (EuMC) and is also conference co-chair of the IEEE International Microwave Biomedical Conference (IMBioC).